Volume 22
Number 9
7 March 2020
Pages 1489–1676

CrystEngComm

rsc.li/crystengcomm

Themed issue: Crystal Engineering for Electrochemical Applications

ISSN 1466-8033

ROYAL SOCIETY OF CHEMISTRY

PAPER
Maria Crespo, Magdalena Titirici *et al.*
Investigating the effects of activating agent morphology on the porosity and related capacitance of nanoporous carbons

CrystEngComm

ROYAL SOCIETY OF CHEMISTRY

PAPER

View Article Online
View Journal | View Issue

Cite this: *CrystEngComm*, 2020, **22**, 1560

Investigating the effects of activating agent morphology on the porosity and related capacitance of nanoporous carbons†

Servann Hérou, Maria Crespo* and Magdalena Titirici *

The increasing interest in nanostructured porous carbon materials in the field of energy storage and electrocatalysis has led to drastic improvement in their properties. These materials are still expensive to manufacture, often due to the harsh chemical treatments required to enhance porosity. In this article, we demonstrate that the process of activating carbons does not uniquely depend on the amount of activating agent (NaOH) but also on the contact area between the salt and the carbonaceous framework to be activated. We compare the microstructure, double layer capacitance and microporosity of carbon materials of the same chemical composition but obtained through two different protocols: electrospinning, which allows the formation of small NaOH domains (~60 nm) homogeneously distributed across lignin fibres, and standard activation, which leads to the growth of larger NaOH domains within the lignin framework. As intimate contact between both phases ensures maximum activation, our electrospun material shows a remarkable capacitance (~180 F g^{-1}) in comparison to the material prepared through standard "mix and dry" activation procedure (~10 F g^{-1}). This is attributed to the generation of micropores (~670 m^2 g^{-1}), tailored from the small activating salt template domains in intimate contact with the lignin framework. In summary, through this work we establish a relationship between the activating agent's morphology and its effect in porosity and energy storage performance. We present a facile method to interpenetrate the chemical activating agent within the carbon precursor structure before pyrolysis, through the efficient usage of the activating agent.

Received 27th October 2019,
Accepted 2nd January 2020

DOI: 10.1039/c9ce01702j

rsc.li/crystengcomm

Introduction

Nanoporous carbons can be synthesised from low-cost precursors and through a myriad of protocols that enable tailored surface areas, specific functional groups and high electrical conductivities.[1,2] The rising importance of these versatile materials as high-performance electrodes for batteries and supercapacitors calls for the development of more efficient synthesis pathways and a better understanding of their structural properties.

Nanoporous carbons have been traditionally prepared through sol–gel synthesis,[3–5] hard/soft templating[6–8] and activation.[9,10] While sol–gel synthesis allows for the development of both micro (<2 nm) and mesoporosity (2–50 nm), hard/soft templating usually uses inorganic nanoparticles and thermo-degradable polymers that generate predominantly mesopores.[4,8]

Activation instead, is performed by the gasification of the carbon itself *via* the reduction of activating alkali and transition-metal salts or oxidizing gases to etch the carbon surface. Chemical activation using KOH or NaOH is one of the most effective way to enhance microporosity in a short time.[11–14] Pores below 2 nm are especially attractive for electrostatic charge storage applications (*e.g.* supercapacitors) where very high surface areas and pore sizes matching that of the electrolyte ions are needed. This type of porosity has been normally controlled by tuning the ratio of carbon to templating/activating agent during the pyrolysis-activation process.[15] Since high porosities are usually achieved with large excess of activating agents[10,15] it is of general interest to propose alternative activation routes that enable high microporosity degrees while maintaining a low usage of salt.

Alkali salts (*e.g.* KOH and NaOH) are frequently used as activation agents. They are first dissolved together with the carbon precursors and annealed after solvent removal. Carbonisation occurs alongside the formation of molten-salt and/or C-metal oxide intermediates. As temperature increases, the inorganic alkali domains within the emerging carbonaceous framework play a double role: they first serve as hard-templates that then activate the carbon surface they

Chemical Engineering Department, Imperial College London, South Kensington, London, SW7 2AZ UK. E-mail: m.crespo-ribadeneyra@imperial.ac.uk

† Electronic supplementary information (ESI) available. See DOI: 10.1039/c9ce01702j

are in contact with by oxidation.[13,16] Here we study this relationship by linking the resulting carbons porosity and the morphology/crystallinity of the activating agent domains prior to carbonisation. We propose the use of electrospinning, a process in which the solvent evaporation rate is particularly high, as a technique that can drastically increase the porosity of lignin-based carbon materials by limiting the crystal size of the templating/activating agent.[17] In contrast to standard techniques used for activation, we were able to produce highly porous carbons with a surface area of 640 m^2 g^{-1} and pore volume of 0.3 cm^{-3} g^{-1}, using 40 times less activating salt than most procedures.[10–13,15–20]

To illustrate our example, we have chosen lignin as carbon precursor — an abundant and environmentally friendly biopolymer that is commonly extracted from wood as a by-product of paper industry. Lignin is an attractive precursor for carbon materials since it enables relatively high yields upon carbonisation. Activated carbons from lignins have been extensively prepared[15,21–28] but the degree of control of their porosity *via* activation is poor compared to the one obtained using carbohydrates as carbon precursors,[13,19,29–32] mainly due to the 3D complexity of its structure. Here, we prepare carbon nanofiber (CNF) mats which, due to the low content of salt that we use for the *in situ* activation of the electrospun lignin, remain structurally intact upon carbonisation and therefore are suitable as free-standing electrodes. Furthermore, the CNFs present a very narrow pore size distribution (between 0.4 nm and 0.75 nm), ideal for charge storage in supercapacitors.[33,34] For the sake of comparing our material to a standard carbon, we also prepared a non-electrospun activated carbon cast film using the same lignin-based solution. After carbonisation, this material was brittle and could not be used as a free-standing electrode but as a powder (AC powder). Through this comparison we show that the porosity of any activated material is determined by the activating salt-carbon precursor interaction during carbonisation. In turn, this relationship also controls the charge storage capacity of the produced carbon. Decreasing the crystallite size of the activating salt during carbonisation was proved to increase by a factor of 10 the microporous surface area and by a factor 10 the maximum energy density.

Results and discussion

Lignin/polymer nanofiber mats were obtained by electrospinning organosolv lignin (90 wt%, see characterisation in Fig. S1–S9, ESI†) and poly-ethylene oxide (PEO, 10 wt%) in a 0.5 M NaOH aqueous solution (see Experimental section for further details). Our typical recipe has a salt : carbon ratio of 0.13, in contrast to most classical activation strategies in which this ratio is above 1. After electrospinning, the material is carbonised under nitrogen at 800 °C to yield mats of porous CNFs which are rich in oxygen-containing groups (5.5 wt% as determined by X-ray photoelectron spectroscopy, see Fig. S10 in ESI†).

NaOH was preferred as activating agent over the widely used KOH for various reasons. First, its lower cost and much larger worldwide production rate than KOH make it more attractive for industrial scale applications.[35,36] Secondly, NaOH activation process is milder than with KOH and thus better maintains the morphology of the free-standing material upon carbonisation. Finally, NaOH is particularly suitable for less ordered carbon materials such as raw biomass or lignin since it reacts with the most energetic sites of the carbon surface.[14,37] During the activation process, the intercalation of Na ions produced during carbothermal reduction promotes the formation of porosity after being washed away from the carbon structure. Since Na does not intercalate easily into ordered structures, it is a particularly effective activating agent for disordered carbonaceous systems.

Scanning electron micrographs (SEM) of the as-spun CNF before carbonisation (Fig. 1a) show typical electrospun narrow-diameter fibres (av. 490 nm) displaying homogeneously distributed brighter features of *ca.* 60 nm in size (see Fig. S9 in ESI†). These regions can be attributed to the nucleation of the activating agent (NaOH) within the precursor solution as the electrospinning proceeds. Their limited size is a consequence of the fast solvent evaporation kinetics: during electrospinning, the polymer solution jet suffers a pronounced elongation which results in a high solvent evaporation rate and a sudden increase in the sodium hydroxide concentration.[38] When the nanofibers reach the current collector, the salt concentration has surpassed the solubility limit. The Na salt then nucleates inside and on the

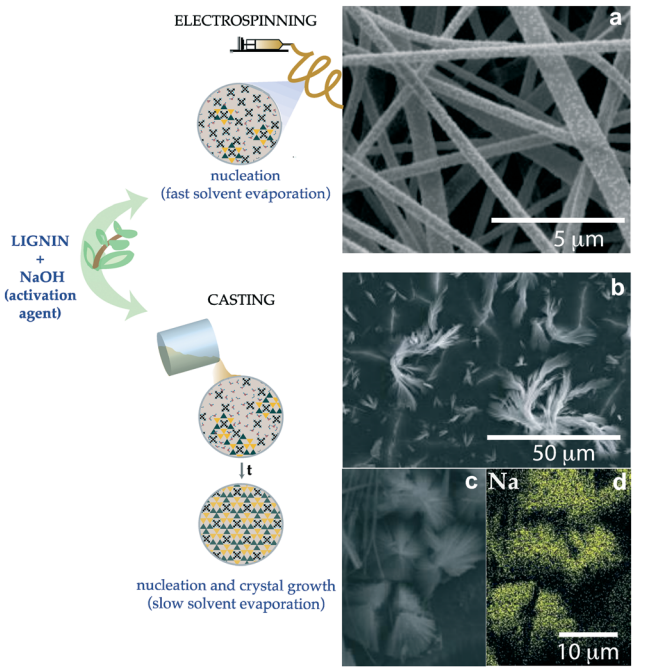

Fig. 1 Scheme of the electrospinning *versus* casting techniques used. (a) SEM of the as-spun polymer nanofibers; (b) SEM of the cast-solution after drying; (c) SEM of the large crystals on the surface and (d) energy-dispersive X-ray spectroscopy mapping on the large crystals (EDX).

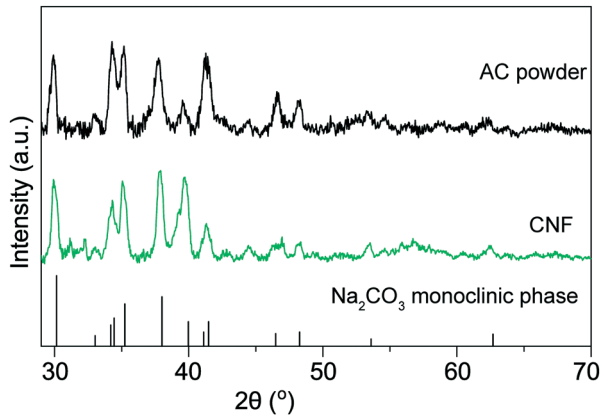

Fig. 2 X-Ray diffraction patterns of the cast powder and electrospun polymer nanofibers before pyrolysis. The natrite pattern (monoclinic Na_2CO_3) was obtained from the ICDD crystallographic database, reference code: 00-037-0451.

surface of the nanofibers (Fig. 3a and b) and since the solvent evaporation occurs in less than 10 milliseconds,[17] further growth of salt crystals is prevented.

In contrast to the electrospun material, the AC powder, prepared by casting the same lignin-PEO/NaOH solution and drying at 110 °C for 30 min, presents micro-sized star-like features (Fig. 1b) with a broad distribution of sizes (between 1 and 50 μm). This suggests that these Na-rich regions (Fig. 1c and d) have nucleated and the crystal growth has been thermodynamically facilitated by the slow solvent evaporation rate of the process. SEM images of both as-spun CNF and AC powder materials before carbonisation are provided in the ESI† (Fig. S8). The drastic morphology difference of the activating agent between these samples emphasises the role of electrospinning as a micro/nano structure-directing technique.

X-ray diffraction patterns of both materials before carbonisation confirmed the presence of monoclinic phase Na_2CO_3 (Fig. 2), confined in a broad amorphous halo due to the presence of disordered carbonaceous matter. The formation of Na_2CO_3 might be explained by the saturation of the solution with CO_2 and the consequent carbonation of the $NaOH_{(aq)}$.[39] However, the presence of an amorphous NaOH phase is not excluded in the two materials.

After carbonisation, the CNF electrospun material has a relatively high microporosity (S_{DR} above 500 $m^2\ g^{-1}$), given the low initial ratio of salt : carbon (Fig. 3a and b). The porosity of the AC powder instead (S_{BET} 60 $m^2\ g^{-1}$ and V_{tot} 0.04 $cm^3\ g^{-1}$), was found to be approximately 10 times lower than that for the CNF (see Table 1). Electrospinning produces nanofibers with a uniform distribution of salt which in turn enhances the interfacial surface between the molten salt and the carbon (Fig. 3d). This optimises the activation during carbonisation and therefore the resulting CNF material is highly porous, with a microporous surface area S_{DR} of 670 $m^2\ g^{-1}$ and a microporous volume of 0.3 g cm^{-3} (see Table 1). In contrast, in the AC powder material, the formation of porosity during pyrolysis is not pronounced since the interfacial contact between the carbon and the salt is confined at the surface (Fig. 3c). This explanation was supported by the comparable carbonisation yields obtained for both samples (Table S1, ESI†), which reveal similar degrees of gasification.

The activation of carbon materials by NaOH and Na_2CO_3 occurs *via* a series of complex cascade reactions between the salt phases and the gases evolved during pyrolysis.[40,41] At low temperatures, the NaOH spontaneously reacts with the evolved CO_2, forming Na_2CO_3 (eqn (1)). Although the Gibbs energy of this reaction decreases with increasing temperature, the increase of the partial pressure of CO_2 during pyrolysis makes it more likely to occur from 350 °C onwards.[42]

$$4NaOH_{(l)} + 2CO_{2(s)} \xrightarrow{\text{from } RT} 2Na_2CO_{3(s)} + 2H_2O_{(g)} \quad (1)$$

At temperatures above 700 °C, the residual presence of NaOH could also oxidise the carbon framework (eqn (2)) forming metallic Na, which tends to react with the reactive sites on the edges of the aromatic domains.[42–44]

$$6NaOH_{(l)} + 2C_{(s)} \xrightarrow{>700\,^{\circ}C} 2Na_{(l)} + 2Na_2CO_{3(s)} + 2H_{2(g)} \quad (2)$$

At these temperatures, the partial thermal decomposition of Na_2CO_3 is also thermodynamically favourable (eqn (3)) and the $CO_{2(g)}$ produced could promote the formation of pores by etching the accessible carbon atoms, as suggested by the Boudouard reaction (eqn (4)).[41]

$$Na_2CO_{3(l)} \xrightarrow{>700\,^{\circ}C} CO_{2(g)} + Na_2O_{(s)} \quad (3)$$

$$CO_{2(g)} + C_{(s)} \xrightarrow{>600\,^{\circ}C} 2CO_{(g)} \quad (4)$$

Similarly to KOH and K_2CO_3, the carbon can also reduce the Na_2CO_3 or Na_2O at temperatures below 1000 °C to form

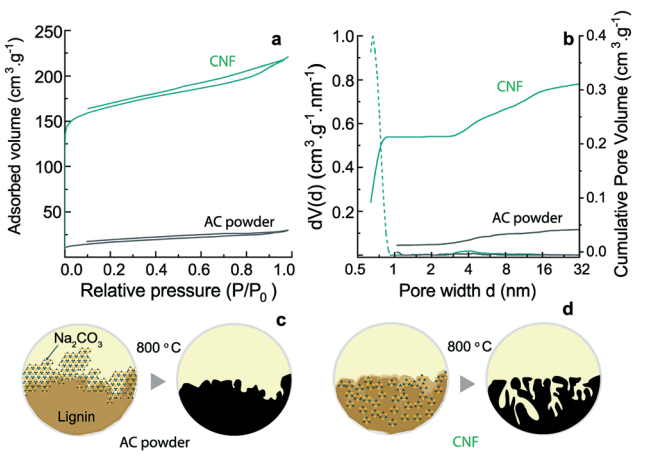

Fig. 3 (a) N_2 sorption isotherms at 77 K of the electrospun CNF and AC powder after pyrolysis; (b) pore size distribution calculated *via* quenched solid density functional theory (QSDFT) model calculated from the adsorption lines of the isotherms. (c and d) Schemes representing the development of porosity during the chemical activation process with Na_2CO_3 for both (c) AC powder and (d) CNF.

Table 1 Surface area data extracted from the N_2 isotherms presented on Fig. 3

	S_{BET} ($m^2\ g^{-1}$)	S_{DR} ($m^2\ g^{-1}$)	V_{DR} ($cm^3\ g^{-1}$)	S_{DFT} ($m^2\ g^{-1}$)	$V_{TOT\ DFT}$ ($cm^3\ g^{-1}$)	$\frac{V_{MICRO}}{V_{TOTAL}}$ (%)	S_{BJH} ($m^2\ g^{-1}$)	V_{BJH} ($cm^3\ g^{-1}$)
CNF	642	689	0.245	312	0.312	68	49	0.094
AC powder	60	66	0.024	56	0.042	33	13	0.023

metallic Na which might also intercalate in-between the aromatic domains formed during pyrolysis (eqn (5) and (6)).[10,31] These two processes, called "carbothermal reduction" gasify the carbon and promotes the formation of porosity.

$$Na_2O_{(s)} + C_{(s)} \xrightarrow{>700\,^{\circ}C} 2Na_{(l)} + CO_{(g)} \quad (5)$$

$$Na_2CO_{3\,(l)} + C_{(s)} \xrightarrow{>700\,^{\circ}C} 2Na_{(l)} + 3CO_{(g)} \quad (6)$$

To illustrate the impact of surface area on energy storage abilities, the two materials were tested as electrodes in supercapacitors, using a two-electrodes symmetric Swagelok cell and 6 M KOH as electrolyte. To minimize the impact of different electrode manufacturing techniques on the electrochemical performances, the AC powder electrodes were also prepared as free-standing films (thickness 120 μm and density of 1.0 ± 0.1 g cm^{-3}). While the cell performances are presented in Fig. 4, we were also able to monitor the polarization of both electrodes *versus* a reference electrode (see Fig. S11a and b, ESI†) to illustrate the relatively symmetric polarization of the cell at low and high scan rate. The capacitive currents were calculated from the cyclo-voltammograms (CVs) and the galvanostatic charge–discharge (GCDs) using the eqn (7) and (8) provided in the Experimental section.

The electrospun CNFs display the typical features of highly capacitive materials, including rectangular CVs at scan rates from 5 mV s^{-1} to 2 V s^{-1} (Fig. 4a and b) and triangular GCD profiles at low and high current densities (Fig. 4c and d). The slight hump in the CVs observed at low cell voltages (from 0 V to 0.9 V) has been previously attributed to the presence of active oxygen-containing functional groups that might contribute to the pseudo-capacitance (see XPS in Fig. S10†).[45,46] The current peak at high over-potential suggests a slight corrosion of the carbon framework due to the higher polarization of the working electrode (see Fig. S11a and b, ESI†). This explains the cyclability just above 90% after 10 000 cycles (Fig. S11f, ESI†).[47] The maximum capacitance, obtained from the GCD profiles, reaches the decent value of 180 F g^{-1} for a single electrode (Fig. 4e), which supports its good performance as supercapacitive material.

As expected, the CVs for the AC powder reveal a much lower capacitive current than its CNF counterpart. The appearance of a reversible redox peak on the CV at low scan-rate and high overpotential (Fig. 4a) could also be either correlated to the reversible protonation of pseudo-capacitive oxygen containing groups (coulombic efficiency of 95%, see Fig. S11d, ESI†).[48] Despite this reversible activity, the maximum capacitance observed for the AC powder is about 10 F g^{-1}, which is nearly 20 times lower than that of CNFs. Accordingly, a much lower discharge time than that for the CNF is observed on the GCD profiles. This very low capacitance at 0.1 A g^{-1} compared to other results found in the literature[20–27] can easily be explained by the low salt : carbon ratio leading to poor micro-porosity development (see Table 1). Electrochemical impedance spectroscopy (EIS) was also performed on the symmetric cell to support the difference in charging mechanisms. The Bode diagram and Nyquist plot (Fig. S11e and f, ESI†) show the phase angle as well as the impedance of the cell at low frequency. As expected, the AC powder does not exhibit the typical

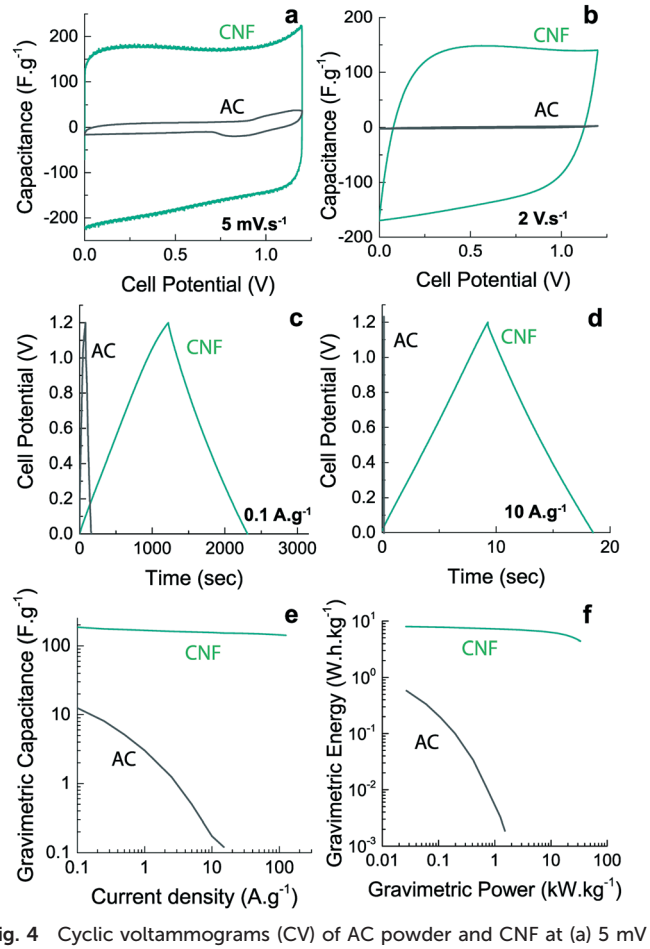

Fig. 4 Cyclic voltammograms (CV) of AC powder and CNF at (a) 5 mV s^{-1} and (b) 2 V s^{-1}; galvanostatic charge discharge (GCD) at (c) 0.1 A g^{-1} and (d) 10 A g^{-1}; (e) capacitance retention between 0.1 A g^{-1} and 150 A g^{-1}; (f) gravimetric Ragone plot.

characteristics of a supercapacitive material. It features a much larger resistance than that of CNF and maintains a phase angle above −60° at 10 mHz. This shows no clear transition from a resistive to a capacitive regime when decreasing the frequency. To support this observation, the relaxation time τ_0 for CNF was calculated. τ_0, the inverse of the frequency ω_0 displaying the maximum in imaginary capacitance C'' (see eqn (9)–(11) in Experimental section), is considered as the characteristic discharge time of the device and is a good tool to compare ionic diffusions in carbon electrodes.[49] CNF exhibited a relaxation time of 370 ms (see Fig. S11g, ESI†). This value is particularly low compared to typical supercapacitive activated carbons, indicating a quick in-micropore ionic diffusion.[31,50] In contrast, AC powder displays a relaxation time infinitely low, due to its very low microporosity.

Finally, the capability of both samples (Fig. 4e and S11c†) reveal a drastic difference in performances resulting from the two contrasting morphologies. CNF exhibits a very high capacitance retention of 75% at 100 A g^{-1} whereas the AC powder has no capacitance beyond 10 A g^{-1}. These results translate into not only an energy density increased by tenfold for CNF but also an extremely high-power capability (Fig. 4f). We explain this phenomenon by the presence of continuous electrical pathways provided by the fibrous network. This probably leads to a higher electrical conductivity than the AC powder material where the electrical resistance between the grains is relatively high.

Conclusions

Using electrospinning, we have synthesised porous carbon nanofibers with a much more efficient chemical activation than carbon materials of the same composition but prepared through standard activation. Through the high intrinsic evaporation rate of the carbon/activating agent solution used for electrospinning, we were able to constrain the growth of the activating agent (Na_2CO_3) domains, and in turn enhance the contact area between the salt and the carbonaceous framework. Therefore, with our electrospun bio-based material, we were able to produce symmetric supercapacitors exhibiting a capacity of 180 F g^{-1} with the relatively low surface area of 670 m^2 g^{-1}, both values surpassing those observed for the material prepared through standard activation.

We have rationalised our observations according to the tailored microporosity we can achieve through electrospinning. When the domain size of the activating agent is limited, the contact area of these and the carbonaceous framework is maximised. This in turn enables higher porosities and the presence of micropores in the resulting carbons. We present a rational method to effectively enhance the microposity of the resulting carbons through the interpenetration of the activating agent within the carbonaceous framework before pyrolysis.

We think that our results will promote further understanding of the chemical activation procedures and the importance of controlling the size/morphology of the activation agent and lead to more efficient material designs.

Experimental procedures

Materials and methods

The organosolv was kindly given to us by the group of Christine Roβberg at the Fraunhofer Center for Chemical-Biotechnological Processes (CBP) in Jena. Sodium hydroxide pellets (NaOH, analytical reagents grade) were purchased from Fisher Scientific. Polyethylene oxide (PEO, M_w 600 000 g mol^{-1}) was purchased from Sigma Aldrich. Both chemicals were used without further purification.

Synthetic procedures

Extraction of the organosolv lignin. Lignin was obtained by organosolv extraction of beech wood, which was first chopped in small pieces and digested at 170 °C during 80 min in a mixture of 50 wt% ethanol/water containing 1% of H_2SO_4. The resulting black liquor was then diluted with H_2O (ratio of 2 : 1 vol/vol water/black liquor) to precipitate the lignin with a yield of 64 wt% with regard to the initial dry wood mass. The lignin obtained from this method contains a very low sulfur content (determined by XPS), low carbohydrate content, a high concentration of syringyl units (determined by nuclear magnetic resonance NMR) and a low molecular weight M_w/M_n/PID of 4815 g mol^{-1}/3207 g mol^{-1}/1.50 *versus* polystyrene (determined by gel permeation chromatography). Lignin characterisation is provided in the ESI.†

Synthesis of carbon nanofibers (CNF). 204 mg of PEO was first dissolved during 2 hours in 15 g of 0.5 M aqueous NaOH solution by stirring. Then 1.84 g of organosolv lignin (OSL) was added and the solution was vigorously stirred for another 2 hours to yield a polymer concentration of 12% wt and a ratio PEO : OSL of 1 : 9. This solution was centrifuged at 10 000 rpm during 5 min to remove the air bubbles present in the solution and facilitate the formation of the Taylor cone during the electrospinning. The solution was then electrospun in a chamber (Nanobox, Plaslab), where temperature was monitored at 22 °C and the relative humidity at 25%. The solution was electrospun at a rate of 2 ml h^{-1} using a 18 gauge needle positively charged at 20 kV. A 25 cm^2 aluminium collector was electrically grounded and placed at 20 cm from the needle. After spinning 4.5 to 5 mL of solution, the mat (approx. 150 μm thickness) is removed from the collector, cut in stripes, sandwiched between two pieces of carbon felt and submitted to heat treatment in a MTI 1200× tubular furnace with 3 heating zones. Carbonisation was performed at 800 °C during 2 h, using a heating rate of 5 °C min^{-1} in the same tubular furnace. Once the carbonisation is performed, the mat is placed in a distilled water bath at room temperature. The temperature of the bath is progressively increased to 85 °C, over the course of 30 min and the temperature is kept constant for 1 hour. This allows the dissolve progressively the remaining salt and

maintain the flexibility of the textile. Then the textile is removed from the bath, rinsed with ethanol and placed in a vacuum oven at 100 °C to dry overnight. The yields observed after thermal treatments are reported in supplementary information. The resulting CNF electrodes exhibit good bending ability over a surface of 50 cm^2, as well as a thickness of approx. 80–120 μm.

Synthesis of cast activated carbon (AC powder). The spinning solution (5 mL) was cast onto a circular (10 cm diameter) glass Petri dish and dried for 30 min at 110 °C in a forced air circulation oven. Subsequently, the film obtained (thickness 1–2 mm) was ground into powder and carbonised under nitrogen at 800 °C during 2 hours, using a heating rate of 5 °C min^{-1}. After carbonisation, the powder was washed at 85 °C in distilled water for a couple of hours, separated by vacuum filtration, rinsed with ethanol and placed in a vacuum oven at 110 °C for drying overnight.

Characterisation

Lignin characterisation. Gel permeation chromatography (GPC) measurements were conducted on an Agilent 1260 infinity system operating in DMF with 5 mM NH_4BF_4 and equipped with refractive index detector and variable wavelength detector, two PLgel 5 μm mixed-C columns (300 × 7.5 mm), a PLgel 5 mm guard column (50 × 7.5 mm) and an autosampler. The instrument was calibrated with linear narrow poly-styrene (PS) standard. The organosolv lignin was dissolved in DMF at a concentration of 1 mg mL^{-1} of solvent, sonicated and filtered through 0.2 μm Nylon filters before analysis. Two-dimensional heteronuclear single quantum coherence (2D-HSQC) (^1H &^{13}C) nuclear magnetic resonance (NMR) spectra were recorded on a Bruker AV-III 600 mHz. The organosolv lignin was dissolved in dimethyl sulfoxide-d6, 99.9 atom% D [$(CD_3)_2SO$] at a concentration of 30 mg mL^{-1} and the resonance signal of residual $(CD_3)_2SO$ at 2.5 ppm (^1H) and 40 ppm (^{13}C) served as reference for the chemical shift δ. ^{31}P NMR spectroscopy was used to quantify the hydroxyl groups after derivatization of lignin with 100 μL of 2-chloro-4,4,5,5-tetramethyl-1,3,2-dioxaphospholane (TMDP).[51–53] The lignin sample (30 mg) was dissolved in dimethylformamide/pyridine (1 : 1 v/v) and mixed with 100 μL of a solution of *N*-hydroxy-5-norbornene-2,3-dicarboxylic acid imide (20 mg mL^{-1}) and chromium(III) acetylacetonate (5 mg mL^{-1}) as internal standard and relaxation agent, respectively. ^{31}P NMR spectra were acquired using an inverse-gated decoupling pulse sequence with a 90 ° pulse angle, 10 s relaxation delay, and 512 scans. Thermogravimetric analysis (TGA) was measured on a Q500 TGA from TA Instrument. The lignin was decomposed at 5 °C min^{-1} under air after being ground in a fine powder. The as-spun mat was cut into small layers and piled on a platinum pan. Between 4 and 5 mg of samples were used for analysis. The differential scanning calorimetry (DSC) was measured in T-zero hermetic aluminium pans (40 μL) on a DSC2500 from TA Instruments. The highly amorphous nature of lignin coupled with its complex hydrogen bonding interactions can induce significant endothermic enthalpy relaxation during the initial DSC scan of the original lignin. During this initial, the sample was first heated from room temperature to 160 °C and maintained at 160 °C for 10 min. The sample was then cooled down to −20 °C with a cooling rate of 10 °C min^{-1} and maintained at this temperature for 10 min. The second heating run was used to determine the glass transition temperature of the sample. The temperature was ramped from −20 °C to 200 °C with a heating rate of 20 °C min^{-1} (as the glass transition is more pronounced at faster heating rates), followed by an isothermal state at 200 °C for 10 min and cooling to room temperature at 30 °C min^{-1}. The sample mass used was approximately 5–6 mg.

Carbon material characterization. The N_2 sorption isotherms were measured at 77 K using a Quantachrome Autosorb instrument. The relative pressure range was measured between 1×10^{-5} and 0.99. This provides information about the pores larger than 0.5 nm. The porosity datas (S_{BET}, S_{DR}, S_{BJH}) reported on Table S1 (ESI†) were measured by the software Novawin. The Brunauer–Emmett–Teller surface area (S_{BET}) was measured over the pressure range of from 5×10^{-3} to 5×10^{-2} for CNF and from 1×10^{-2} to 1×10^{-1} for AC powder. The pore size distribution was calculated from the adsorption line using a quenched-solid model QSDFT assuming slit and cylindrical pores geometries. The mesoporous surface area S_{BJH} was calculated from the adsorption line. The microporous data were calculated from the adsorption line by the Dubinin–Radushkevich model on the relative pressure range from 4×10^{-3} to 1×10^{-2} for CNF and from 5×10^{-2} to 3×10^{-1} for AC powder. Scanning electron microscopy was used to investigate the microstructures of the as-spun CNF and the dried solution. A small but representative amount of sample was fixed onto a steel stub with a sticky carbon tape. All samples were coated with gold (45 seconds, 15 mA plasma current) prior to imaging to avoid charging of electrons within the SEM chamber. Images were taken on a FEI Inspect F instrument using an acceleration voltage of 20 kV and a working distance of 10 cm. Energy-dispersive X-ray spectroscopy, used for elementary composition analysis, was performed on a JEOL InTouchScope model using the same acceleration voltage but a working distance of 15 cm. Prior to imaging, the non-conductive samples were coated with gold. X-Ray diffraction was performed on a silicon wafer on a Bruker D2. The dried-cast solution was finely ground into powder and deposited onto the wafer. The as-spun nanofibers were cut into squares (1 cm sides) and 3 layers were pressed onto the silicon wafer. The spectra were recorded for 10 hours from an angle from 20° to 70°.

Electrochemical measurements. Electrochemical measurements were obtained using a standard 2 electrodes symmetric Swagelok cell connected to a VSP Biologic potentiostat using a Hg/Hg_2SO_4 (in saturated $K_2SO_{4(aq)}$) reference electrode to record the polarization of both electrodes simultaneously (see ESI†). CNF electrodes were

cut from the mat using a hole-punch with a diameter of 7 mm and directly placed on stainless steel current collectors. Free-standing carbon electrodes were manufactured by mixing 90 wt% of our AC powder with 5 wt% of conductive carbon black and 5 wt% of PTFE in absolute ethanol. Ethanol was fully evaporated from the paste at 110 °C and a few drops of ethanol were added to form compact free-standing electrodes. The electrodes were calendered in an electric 2-rolls mill to a thickness of 100–150 μm and punched with a 7 mm diameter. Finally, the electrodes were dried under vacuum at 100 °C overnight. Before assembling the cell, both types of electrodes were wetted by adding a few drops of electrolyte on the electrode and pressing it onto the current collector using a spatula. In this way, the electrolyte can infiltrate properly the macro structure of the electrodes. Cell assembly. The cells were assembled by pressing the 2 electrodes separated by a 10 mm disc glass fibre separator (Whatman) between the 2 current collectors. Prior to measurement, 500 cycles were run at 5 A g^{-1} in order to improve the electrolyte access to the micropores. The capacitance was observed to increase up to 5%. Cyclo-voltammograms (CV) were recorded at various scan rates, galvanostatic charge discharge (GCD) at different current densities and electrochemical impedance spectroscopy (EIS) between 500 kHz and 10 mHz with a signal amplitude of 5 mV. The specific capacitances (F g^{-1}) of a single electrode were calculated from the cyclo-voltammograms (eqn (7)) and the galvanostatic charge discharge (eqn (8)) as following:

$$C_{CV} = \frac{4 \cdot I}{v \cdot m} \tag{7}$$

$$C_{GCD} = \frac{4 \cdot Q}{(\Delta V - IR_{drop}) \cdot m} \tag{8}$$

The relaxation time was calculated from eqn (9):

$$\tau_0 = \frac{1}{\omega_0} \tag{9}$$

ω_0 are $C''(\omega)$ are defined as the following:

$$\frac{dC''(\omega_0)}{d\omega = 0} \tag{10}$$

$$C''(\omega) = \frac{-Z(\omega)}{\omega \cdot |Z(\omega)|^2} \tag{11}$$

The following notations are used: I (mA) current, v (mV s^{-1}) scan rate of the cyclovoltammograms, Q (C) the charge accumulated in the porous material calculated during the discharge cycle, ΔV (V) is the voltage window, IR_{drop} (V) is the voltage drop observed when the current is reverse during GCD, ω (Hz) is the frequency, $Z'(\omega)$ and $Z''(\omega)$ are the real and imaginary parts of the impedance and m (g) is the mass of the working electrode.

Conflicts of interest

The authors declare no competing financial interests.

Acknowledgements

The authors would like to thank Mr. Richard Sweeney, Research Officer at the Diffraction Centre of the Department of Materials, Royal School of Mines, Imperial College London, for his help in obtaining and analysing the XRD spectra. We would also like to acknowledge the help of Dr. Mahmoud Ardakani for his insight in EDS mapping and the use of characterisation facilities within the Harvey Flower Electron Microscopy Suite, Department of Materials, Imperial College London.

References

1 M. Antonietti and K. Müllen, *Adv. Mater.*, 2010, **22**, 787.
2 S. Perkin and J. Klein, *Soft Matter*, 2013, **9**, 10438–10441.
3 S. Dutta, A. Bhaumik and K. C.-W. Wu, *Energy Environ. Sci.*, 2014, **7**, 3574–3592.
4 M. Antonietti, N. Fechler and T. P. Fellinger, *Chem. Mater.*, 2014, **26**, 196–210.
5 H. Tamon, H. Ishizaka, M. Mikami and M. Okazaki, *Carbon*, 1997, **35**, 791–796.
6 L. Borchardt, M. Oschatz and S. Kaskel, *Mater. Horiz.*, 2014, **1**, 157–168.
7 T.-Y. Ma, L. Liu and Z.-Y. Yuan, *Chem. Soc. Rev.*, 2013, **42**, 3977–4003.
8 L. Chuenchom, R. Kraehnert and B. M. Smarsly, *Soft Matter*, 2012, **8**, 10801.
9 A. G. Pandolfo and A. F. Hollenkamp, *J. Power Sources*, 2006, **157**, 11–27.
10 J. Wang and S. Kaskel, *J. Mater. Chem.*, 2012, **22**, 23710.
11 Y. Zhai, Y. Dou, D. Zhao, P. F. Fulvio, R. T. Mayes and S. Dai, *Adv. Mater.*, 2011, **23**, 4828–4850.
12 K. V. Kumar, S. Gadipelli, K. Preuss, H. Porwal, T. Zhao, Z. X. Guo and M. M. Titirici, *ChemSusChem*, 2017, **10**, 199–209.
13 N. Fechler, T. P. Fellinger and M. Antonietti, *Adv. Mater.*, 2013, **25**, 75–79.
14 A. Perrin, A. Celzard, A. Albiniak, J. Kaczmarczyk, J. F. Marêché and G. Furdin, *Carbon*, 2004, **42**, 2855–2866.
15 H. Lu and X. S. Zhao, *Sustainable Energy Fuels*, 2017, **1**, 1265–1281.
16 N. Díez, G. A. Ferrero, A. B. Fuertes and M. Sevilla, *Batteries Supercaps*, 2019, **2**, 701–711.
17 A. Greiner and J. H. Wendorff, *Angew. Chem., Int. Ed.*, 2007, **46**, 5670–5703.
18 J. Yan, Q. Wang, T. Wei, L. Jiang, M. Zhang, X. Jing and Z. Fan, *ACS Nano*, 2014, **8**, 4720–4729.
19 M. Sevilla and A. B. Fuertes, *ChemSusChem*, 2016, **9**, 1880–1888.

20 L. L. Zhang, X. Zhao, M. D. Stoller, Y. Zhu, H. Ji, S. Murali, Y. Wu, S. Perales, B. Clevenger and R. S. Ruoff, *Nano Lett.*, 2012, **12**, 1806–1812.
21 D. Salinas-Torres, R. Ruiz-Rosas, M. J. Valero-Romero, J. Rodríguez-Mirasol, T. Cordero, E. Morallón and D. Cazorla-Amorós, *J. Power Sources*, 2016, **326**, 641–651.
22 D. Saha, Y. Li, Z. Bi, J. Chen, J. K. Keum, D. Hensley, A. Grappe, H. M. Meyer, S. Dai, M. P. Paranthaman, A. K. Naskar, K. Dale, H. A. Grappe, H. M. M. Iii and M. Parans, *Langmuir*, 2014, **30**, 900–910.
23 D. Kai, M. J. Tan, P. L. Chee, Y. K. Chua, Y. L. Yap and X. J. Loh, *Green Chem.*, 2016, **18**, 1175–1200.
24 W. Zhang, H. Lin, Z. Lin, J. Yin, H. Lu, D. Liu and M. Zhao, *ChemSusChem*, 2015, **8**, 2114–2122.
25 J. M. Rosas, R. Berenguer, M. J. Valero-Romero, J. RodrÃguez-Mirasol and T. Cordero, *Front. Mater.*, 2014, **1**, 1–17.
26 V. Fierro, V. Torné-Fernández and A. Celzard, Highly microporous carbons prepared by activation of kraft lignin with KOH, *Studies in Surface Science and Catalysis*, 2007, vol. 160, pp. 607–614, DOI: 10.1016/S0167-2991(07)80078-4.
27 C. M. Fierro, J. Górka, J. A. Zazo, J. J. Rodriguez, J. Ludwinowicz and M. Jaroniec, *Carbon*, 2013, **62**, 233–239.
28 B. Yu, Z. Chang and C. Wang, *Mater. Chem. Phys.*, 2016, **181**, 187–193.
29 M.-M. Titirici, R. J. White, C. Falco and M. Sevilla, *Energy Environ. Sci.*, 2012, **5**, 6796.
30 A. B. Fuertes, G. A. Ferrero, N. Diez and M. Sevilla, *ACS Sustainable Chem. Eng.*, 2018, **6**(12), 16323–16331.
31 A. B. Fuertes and M. Sevilla, *ACS Appl. Mater. Interfaces*, 2015, **7**, 4344–4353.
32 R. J. White, V. Budarin, R. Luque, J. H. Clark and D. J. Macquarrie, *Chem. Soc. Rev.*, 2009, **38**, 3401.
33 N. Jackel, P. Simon, Y. Gogotsi and V. Presser, *ACS Energy Lett.*, 2016, **1**, 1262–1265.
34 J. Chmiola, C. Largeot, P. L. Taberna, P. Simon and Y. Gogotsi, *Angew. Chem., Int. Ed.*, 2008, **47**, 3392–3395.
35 M. A. Lillo-Ródenas, D. Lozano-Castelló, D. Cazorla-Amorós and A. Linares-Solano, *Carbon*, 2001, **39**, 751–759.
36 R. E. K.-O. Kirk-Othmer, *Encyclopedia of Chemical Technology*, 57th edn, 2007.
37 E. Raymundo-Piñero, P. Azaïs, T. Cacciaguerra, D. Cazorla-Amorós, A. Linares-Solano and F. Béguin, *Carbon*, 2005, **43**, 786–795.
38 C. B. Giller, D. B. Chase, J. F. Rabolt and C. M. Snively, *Polymer*, 2010, **51**, 4225–4230.
39 S. J. Mun, S. J. Han and J. H. Wee, *Energy Fuels*, 2018, **32**, 8614–8622.
40 D. A. Fox and A. H. White, *Ind. Eng. Chem.*, 1931, **23**, 259–266.
41 P. Delhaes, *Carbon-based Solids and Materials*, 2013.
42 M. A. Lillo-Ródenas, D. Cazorla-Amorós and A. Linares-Solano, *Carbon*, 2003, **41**, 267–275.
43 Y. Yamashita and K. Ouchi, *Carbon*, 1982, **20**, 47–53.
44 J. C. C. Freitas, M. A. Schettino, F. G. Emmerich, A. Wong and M. E. Smith, *Solid State Nucl. Magn. Reson.*, 2007, **32**, 109–117.
45 Y. Zhao, W. Ran, J. He, Y. Song, C. Zhang, D. B. Xiong, F. Gao, J. Wu and Y. Xia, *ACS Appl. Mater. Interfaces*, 2015, **7**, 1132–1139.
46 Y. J. Oh, J. J. Yoo, Y. I. Kim, J. K. Yoon, H. N. Yoon, J. H. Kim and S. B. Park, *Electrochim. Acta*, 2014, **116**, 118–128.
47 M. He, K. Fic, E. Frackowiak, P. Novák and E. J. Berg, *Energy Environ. Sci.*, 2016, **9**, 623–633.
48 S. Chaleawlert-umpon and C. Liedel, *J. Mater. Chem. A*, 2017, **5**, 24344–24352.
49 P. L. Taberna, P. Simon and J. F. Fauvarque, *J. Electrochem. Soc.*, 2003, **150**, A292.
50 A. B. Fuertes and M. Sevilla, *ChemSusChem*, 2015, **8**, 1049–1057.
51 A. Granata and D. S. Argyropoulos, *J. Agric. Food Chem.*, 1995, **43**, 1538–1544.
52 J. Rönnols, H. Schweinebarth, A. Jacobs, J. S. Stevanic, A. Olsson and A. Reimann, *Nord. Pulp Pap. Res. J.*, 2015, **30**, 550–561.
53 Y. Pu, S. Cao and A. J. Ragauskas, *Energy Environ. Sci.*, 2011, **4**, 3154–3166.